JOURNAL OF GEOPHYSICAL RESEARCH, VOL. 106, NO. C11, PAGES 26,899–26,915, NOVEMBER 15, 2001

On the dynamics of internal waves in a nonlinear, weakly nonhydrostatic three-layer ocean

Angelo Rubino

Dipartimento di Scienze Ambientali dell'Università Ca' Foscari di Venezia, Venice, Italy

Peter Brandt

Institut für Meereskunde an der Universität Kiel, Kiel, Germany

Rainer Weigle

Deutsches Klimarechenzentrum, Hamburg, Germany

Abstract. Aspects of the dynamics of internal solitary waves evolving in a three-layer ocean are investigated using a new numerical multilayer model that solves the nonlinear, weakly nonhydrostatic Boussinesq equations and uses high-resolution in situ data. The model applications refer to two different phenomena frequently observed in the real ocean, which can be described using a three-layer model rather than a two-layer model. In the first application the influence of the strength of a shallow seasonal thermocline superimposed on a two-layer permanent stratification on the structure of internal solitary waves is studied. It is found that while for small to medium wave amplitudes a decrease in the strength of the thermocline yields an increase in the simulated wavelengths, for large wave amplitudes this dependence is no longer monotonic. In particular, in the limiting case of a vanishing thermocline, first-mode internal solitary wave solutions of the three-layer numerical model tend to the analytical internal solitary wave solutions of the Miyata equations, a two-layer model, in which the full nonlinearity of the shallow-water theory up to first-order phase dispersion is retained. In the second application that refers particularly to high-resolution observations made north and south of the Strait of Messina in the Eurafrican Mediterranean basin the generation of internal solitary waves by the evolution of surface and subsurface water jets is investigated. The analysis of the in situ data shows in fact that from very energetic surface and subsurface jet-like disturbances subject to strong turbulent mixing internal solitary waves emerge as robust, quasi-nondissipative oceanic features. Idealized flow conditions aimed at approximating possible initial stages of the observed water jets are imposed to force our numerical model. In general, good agreement is found between characteristics of observed and simulated wave fields. Our investigation identifies the observed water jets as peculiar features of the complex ocean dynamics and suggests that layered numerical models can represent helpful tools in understanding fundamental processes inherent in their intricate dynamics.

1. Introduction

In the past 2 decades the number of papers reporting observations of oceanic internal solitary waves has dramatically increased [*Ostrovsky and Stepanyants*, 1989; *Apel et al.*, 1995]. Such a remarkable proliferation can be ascribed particularly to the continuously increasing amount of available high-resolution remote sensing data of the sea surface showing manifestations of internal solitary waves. These oceanic features are in fact visible at the sea surface because they are associated with horizontally varying surface currents that modulate the local oceanic surface wave spectrum [*Alpers*, 1985]. As a consequence of the acknowledgment of the ubiquity of the internal solitary waves in the world's oceans, in the past few years the number of theoretical studies and experimental investigations on topics related to the dynamics of internal solitary waves has experienced a substantial increase. In particular, theoretical studies on internal solitary waves often have been carried out using hydrodynamical numerical models [*Lamb and Yan*, 1996; *Brandt et al.*, 1996, 1997; *Grimshaw et al.*, 1997; *Terez and Knio*, 1998; *Brown and Christie*, 1998; *Holloway et al.*, 1999; *Vlasenko et al.*, 2000] which, in general, can be classified into two broad categories: layered and continuously stratified models. Continuously stratified models can allow a complete description of the fully nonlinear, nonhydrostatic dynamics of internal solitary waves [*Lamb and Yan*, 1996; *Terez and Knio*, 1998; *Vlasenko et al.*, 2000]. However, because of the complexity inherent in the numerical methods necessary to solve their governing equations, which can result in an unsustainedly large computational effort, their performances are often limited, especially as far as the

Paper number 2001JC000958.
0148-0227/01/2001JC000958.

dynamics of internal disturbances evolving over long distances is concerned. In addition, the extraction of valuable information from a usually intricate picture provided by these models can represent a very complex task. For these reasons the alternative approach (which corresponds, indeed, to the first approach to the numerical simulation of oceanic internal solitary waves) consists in describing the evolution of these oceanic features in the frame of a dynamical system based on the assumption of a two-layer ocean [*Djordjevic and Redekopp,* 1978; *Koop and Buttler,* 1981; *Gerkema,* 1996; *Brandt et al.,* 1996, 1997]. The advantage of using layered models lies in their dynamical simplicity, which allows for a straightforward diagnosis of the processes retained. At the same time they are dynamically sophisticated enough to simulate realistically different oceanographic phenomena [*McCreary et al.,* 1997]. Using this approximation, several studies have been carried out that demonstrate that considering a two-layer system suffices for the description of the main characteristics of internal solitary waves observed in the ocean, as the improvement brought by considering a more complex stratification is often only marginal. However, there are several phenomena related to internal solitary wave dynamics that cannot be addressed using a two-layer model, although they can be accurately described by layered models with more than two layers. In several locations of the world's oceans, for instance, superimposed on a permanent two-layer stratification, during most of the year a shallow seasonal thermocline is present that modifies the structure of the internal solitary waves travelling along the boundaries between the two permanent water masses and that may even constitute the main wave guide along which internal solitary waves propagate. In other locations of the world's oceans the dynamics of the local internal wave field is intrinsically linked to the presence of intrusions of one water mass between two different water masses [*Brandt et al.,* 1999]. There are regions where both phenomena can occur. For instance, in the Strait of Messina, located in the Eurafrican Mediterranean basin, the existence of tidally induced internal solitary waves is well documented [*Alpers and Salusti,* 1983; *Griffa et al.,* 1986; *di Sarra et al.,* 1987; *Sapia and Salusti,* 1987; *Artale et al.,* 1990; *Nicolò and Salusti,* 1991; *Brandt et al.,* 1997, 1999]. In the Strait of Messina, two different water masses are encountered throughout the year: the Modified Atlantic Water and the deeper Levantine Intermediate Water. During most of the year, superimposed on this vertical stratification is a strong, shallow seasonal thermocline [*Brandt et al.,* 1997]. On the other hand, the Strait of Messina is characterized by the presence, along its axis, of strong horizontal density gradients [*Defant,* 1940, 1961]. In the near-surface layer the water density is, in general, larger in the southern than in the northern part of the strait, although there is evidence that this climatological distribution undergoes strong changes: During October 1995, *Brandt et al.* [1999] observed, in fact, a reversal of the climatological horizontal density distribution in the near-surface water of the Strait of Messina. However, whenever a horizontal density gradient along the strait exists, surface and subsurface water jets can be generated by the action of the strong semidiurnal tide, from which large-amplitude internal solitary waves may evolve. In the initial stage of their evolution these jets appear as energetic features characterized by regions of enhanced vertical shear velocity where intense mixing can occur. However, the internal solitary waves produced by these disturbances appear as very robust features that propagate without appreciable energy loss. The dynamics of the flow features discussed in the two examples quoted above cannot be addressed using a two-layer oceanic model, but it can be described very simply and accurately using a three-layer oceanic model.

The paper is organized as follows: In section 2 the numerical model is described. In section 3, general characteristics of first-mode internal solitary waves in a three-layer system are discussed. In section 4, tidally induced surface and subsurface jets are presented. In section 5, processes related to the dynamics of internal solitary waves emerging from bore-like water jets are investigated numerically. Finally, in section 6, conclusions are presented.

2. Model Theory

The model used in the present investigation is a three-layer model, as schematically depicted in Figure 1. In Figure 1, D denotes the water depth, and h_i $(i = (1,2,3))$ is the layer thickness of each layer. The displacement of the interface between the surface and the intermediate layer is denoted by ζ_1, and the displacement of the interface between the intermediate and the bottom layer is denoted by ζ_2. Our model is a Boussinesq model capable of describing nonlinear, weakly nonhydrostatic internal waves of large amplitudes. The model equations represent an extension to a three-layer model of the two-layer model presented by *Brandt et al.* [1996]. As in that case, the equations are derived in accordance to the work of *Mei* [1983], who derived corresponding equations for a single-layer fluid. The governing equations read

$$\frac{\partial \bar{u}_2}{\partial t} + \bar{u}_2 \frac{\partial \bar{u}_2}{\partial x} - \frac{\partial \bar{u}_1}{\partial t} - \bar{u}_1 \frac{\partial \bar{u}_1}{\partial x} + g'_1 \frac{\partial \zeta_1}{\partial x} - A_H \frac{\partial^2 \bar{u}_2}{\partial x^2} + A_H \frac{\partial^2 \bar{u}_1}{\partial x^2} - \frac{h_2^2}{3} \frac{\partial^3 \bar{u}_2}{\partial t \partial x^2} + \frac{h_1^2}{3} \frac{\partial^3 \bar{u}_1}{\partial t \partial x^2} - \frac{h_2 h_3}{2} \frac{\partial^3 \bar{u}_3}{\partial t \partial x^2} = 0, \quad (1)$$

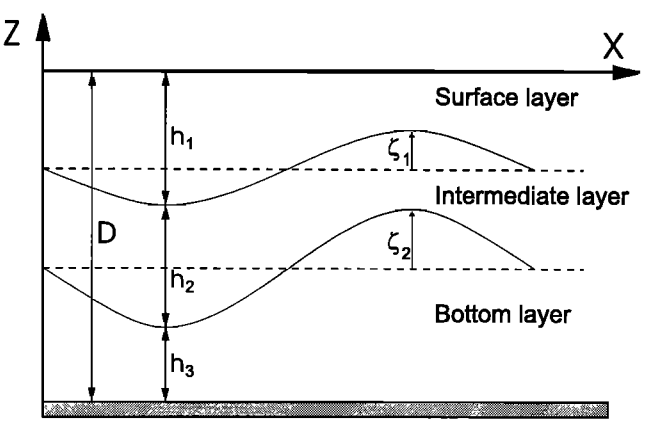

Figure 1. Schematic plot of the three-layer system. Here D denotes the water depth, and h_i $(i = (1,2,3))$ is the layer thickness, ζ_1 is the displacement of the interface between the surface and the intermediate layer, and ζ_2 is the displacement of the interface between the intermediate and the bottom layer.

$$\frac{\partial \bar{u}_3}{\partial t}+\bar{u}_3\frac{\partial \bar{u}_3}{\partial x}-\frac{\partial \bar{u}_2}{\partial t}-\bar{u}_2\frac{\partial \bar{u}_2}{\partial x}+g'_2\frac{\partial \zeta_2}{\partial x}-A_H\frac{\partial^2 \bar{u}_3}{\partial x^2}$$
$$+A_H\frac{\partial^2 \bar{u}_2}{\partial x^2}-\frac{h_3^2}{3}\frac{\partial^3 \bar{u}_3}{\partial t\partial x^2}+\frac{h_2^2}{3}\frac{\partial^3 \bar{u}_2}{\partial t\partial x^2}+\frac{h_2h_1}{2}\frac{\partial^3 \bar{u}_1}{\partial t\partial x^2}=0, \quad (2)$$

$$\frac{\partial \zeta_1}{\partial t}-\frac{\partial}{\partial x}(h_1\bar{u}_1)=0, \quad (3)$$

$$\frac{\partial \zeta_2}{\partial t}+\frac{\partial}{\partial x}(h_3\bar{u}_3)=0, \quad (4)$$

$$\frac{\partial}{\partial x}(h_1\bar{u}_1+h_2\bar{u}_2+h_3\bar{u}_3)=0. \quad (5)$$

Here $\bar{u}_i$ $(i = 1,2,3)$ represents the vertically averaged water velocity within each layer, g'_i $(i = 1,2)$ is the reduced gravity (defined as $g'_i = g\Delta\rho_i/\bar{\rho}_i$, where g is the gravity acceleration, $\Delta\rho_i = \rho_{i+1} - \rho_i$ is the density difference between the layer i and the layer $i+1$, and $\bar{\rho}_i = (\rho_i + \rho_{i+1})/2$ is the average density of the two layers i and $i+1$), and A_H is the horizontal momentum diffusion coefficient.

Equations (1)-(5) are obtained from a perturbation expansion of the Laplace equations for the velocity potentials in a three-layer system in which shallow-water and small-wave amplitude are assumed; that is, the governing equations are valid when both expansion parameters $\mu^2 = k^2H^2$ and $\varepsilon = aH^{-1}$ are small against 1. Here a and k denote the wave amplitude and wavenumber, respectively, and H denotes a typical vertical length scale of the density stratification. Our model retains all the purely nonlinear terms. Note that in our expansion, only terms of $O(\varepsilon)$ are present, which, however, would result also in higher-order nonlinear terms by deriving, starting from our equations, a single-evolution equation analogous to the Korteweg-de Vries equation. The model retains also first-order dispersive terms (terms of $O(\mu^2)$), but it neglects mixed nonlinear-dispersive terms as well as higher-order dispersive terms (terms of $O(\varepsilon\mu^2, \mu^4, \ldots)$). Thus, in effect, the small-amplitude approximation is used only in the dispersive terms.

Equations (1)-(5) are discretized on a staggered Arakawa C-grid, and the time stepping is performed by an implicit two-time level scheme. In our model we have neglected the Coriolis force, interface, and bottom friction. Horizontal eddy diffusion is instead retained in our numerical model in order to ensure numerical stability. Our numerical model can be also used to describe a two-layer system. In that case only (1), (3), and (5) with $h_3 \equiv 0$ and $\bar{u}_3 \equiv 0$ are solved.

3. Structure of Internal Solitary Waves in a Three-Layer Ocean

In the present section the structure of internal solitary waves is investigated in a three-layer ocean composed of a shallow seasonal thermocline superimposed on a permanent two-layer stratification, a situation often observed in the world's oceans. Numerical simulations were performed assuming a flat bottom ocean of 1000 m depth having a lower interface located at 150 m depth and an upper interface located at 50 m depth. The investigation was carried out by varying the values of the water density within the three different layers. To achieve this goal, we used the following scheme: The relative density difference at the lower interface was set to $m \times 2.0 \times 10^{-3}$, where m is a parameter belonging to the interval $0 \le m \le 1$. The relative density difference at the upper interface was then calculated to give a constant phase speed of the linear first-mode internal waves of 1.58 m s^{-1} (a derivation of first-mode and second-mode phase speeds for linear internal waves propagating in a three-layer ocean is presented in Appendix A). Thus, for example, $m = 0$ results in a two-layer system in which the interface is located at 50 m depth and the relative density difference is 5.37×10^{-3}, while $m = 1$ results in a two-layer system in which the interface is located at 150 m depth and the relative density difference is 2.0×10^{-3}. The resulting density distributions can be considered also as possible schematizations of oceanic vertical stratifications found near the Strait of Messina in the Eurafrican Mediterranean basin (see also section 1). In our simulations we used five different values of m: The resulting relative density differences are listed in Table 1. To initialize our numerical model, we used ad hoc disturbances of the interface displacements as well as of the velocity fields, which turned out to develop rapidly into form-preserving internal solitary waves. In order to minimize the size of our computational domain we referred the simulated disturbances to a Galilean frame moving at the phase velocity of the fastest internal disturbance, which emerged from the initial disturbance. A similar method for deriving numerical internal solitary wave solutions was used by *Vlasenko et al.* [2000]. Note that numerical stability was achieved in the present simulations without requiring the inclusion of horizontal diffusion terms.

Mathematically, the wavelength of a solitary wave is infinite. However, in the literature it is often defined as a typical horizontal length scale referring to aspects of the solitary wave structure like, for example, structure of the pycnocline displacement, distance between maximum horizontal velocity convergence and divergence, or distance between maximum and minimum vertical velocity. From these definitions it is evident that the wavelength of a solitary wave is, in general, a function of the vertical coordinate. A detailed investigation on the dependence of wavelength of large-amplitude internal solitary waves on depth is given by *Vlasenko et al.* [2000]. In the present study we will refer to the wavelength of an internal solitary wave defined as follows:

$$L = -\frac{1}{2A}\int_{-\infty}^{\infty}\zeta_1 dx, \quad (6)$$

where A denotes the amplitude (crest to trough) of the solitary wave at the upper interface. Figure 2 shows the amplitude-

Table 1. Values of m (See Text) and Corresponding Relative Density Differences at the Upper interface ($\Delta\rho_1/\bar{\rho}_1$) and at the Lower Interface ($\Delta\rho_2/\bar{\rho}_2$) Used for the Calculation of Internal Solitary Wave Parameters by our Numerical Model

Number	m	$\Delta\rho_1/\bar{\rho}_1$	$\Delta\rho_2/\bar{\rho}_2$
1	0.0	5.37×10^{-3}	0.0
2	0.75	2.8×10^{-3}	1.5×10^{-3}
3	0.87	1.74×10^{-3}	1.74×10^{-3}
4	0.95	0.8×10^{-3}	1.9×10^{-3}
5	1.0	0.0	2.0×10^{-3}

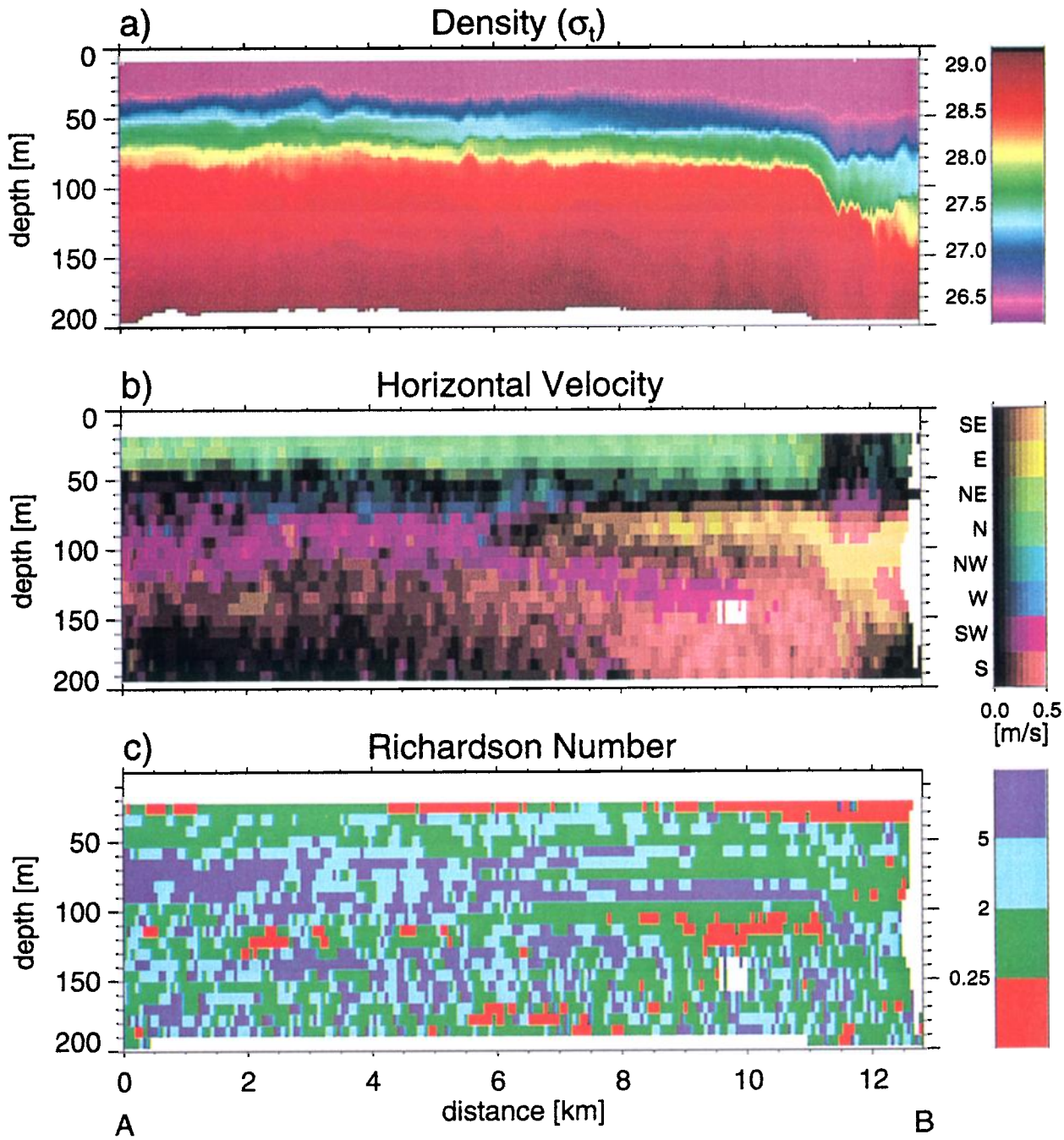

Plate 1. (a) Density distribution measured by the CTD chain, (b) distribution of the horizontal velocity field measured by the ADCP, and (c) distribution of the Richardson number between the positions A and B marked in Figure 3. In Plate 1b the colors represent the different directions of the horizontal velocity, while their brightness represents the velocity strength

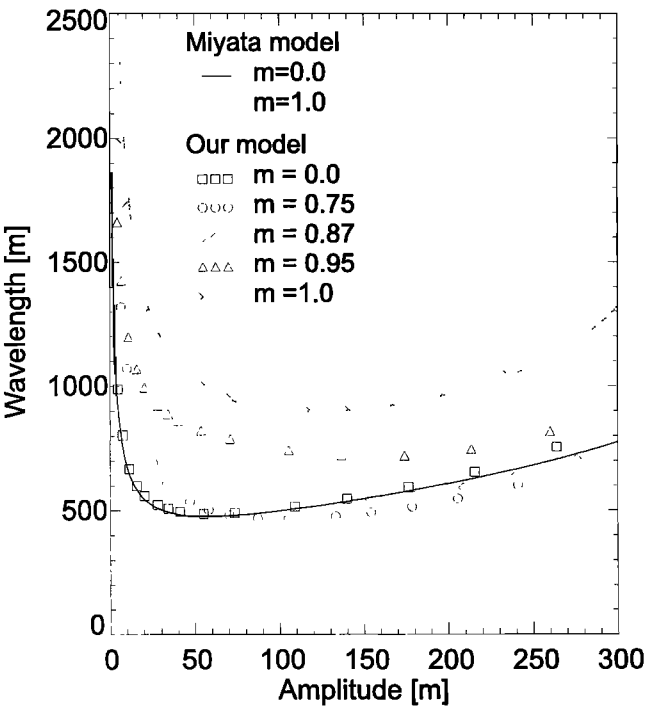

Figure 2. Relation between amplitude and wavelength (defined by (6)) of internal solitary waves as simulated by our model for a three-layer system having undisturbed interfaces located at 50 and 150 m depth for different relative density differences (see Table 1). Also plotted are the relations between amplitude and wavelength of internal solitary waves as simulated by the Miyata model and by our model for a two-layer system having its undisturbed interface located at 50 and 150 m depth and relative density differences of 5.37×10^{-3} and 2.0×10^{-3} (these cases correspond to $m = 0$ and $m = 1$, respectively). Note that for $m = 1$ the wavelengths and the amplitudes of the internal solitary waves were calculated at the interface located at 150 m depth.

wavelength relationship for internal solitary waves simulated by our numerical model using the five different stratifications mentioned above (see Table 1) and derived by the Miyata model, an analytical two-layer model in which the full nonlinearity of the shallow-water theory up to first-order phase dispersion is retained [*Miyata,* 1988], using the two-layer stratifications characterized by $m = 0$ and $m = 1$.

Let us first consider the two limiting cases of a vanishing density difference between the surface and intermediate layers as well as between the intermediate and bottom layers. In the first case the three-layer system degenerates into a two-layer system with a shallow interface; in the second case it degenerates into a two-layer system with a deeper interface. Because of variations in the relative magnitude of the nonlinear and dispersive coefficients, the two-layer Korteweg-de Vries model [see, e.g., *Whitham,* 1974] predicts larger wavelengths in the first rather than in the second case. In both cases the wavelength is a monotonically decreasing function of the amplitude. For small to medium wave amplitudes our model shows a qualitative agreement with the two-layer Korteweg-de Vries model. For increasing amplitudes the distance between our model and the two-layer Korteweg-de Vries model increases. For all wave amplitudes, however, the results provided by our model agree excellently with the results obtained using the Miyata equations. The only difference between the equations on which the two models are based consists in the neglect, in our model, of the combined nonlinear-dispersive terms, which are retained in the Miyata equations. A comparison between the Miyata model and our model can thus be used for testing the appropriateness of the simplifications used in our model as well as for testing the numerical scheme used to solve our model equations. The obtained results confirm that our numerical scheme represents an efficient tool for the discrete solution of the model equations and that the combined nonlinear-dispersive terms play only a minor role in determining the structure of internal solitary waves in a two-layer ocean.

The variation of the density structure of the three-layer model performed in our numerical experiments corresponds to a transition from an internal wave propagation occurring merely along the shallower wave guide ($m = 0$) to a wave propagation occurring merely along the deeper wave guide ($m = 1$). For small to medium wave amplitudes (approximately up to 50 m) a decrease in strength of the thermocline yields an increase in the simulated wavelengths. Thus, in this range of amplitudes, for a given amplitude the corresponding wavelength is largest in the limiting case of a vanishing density difference between surface and intermediate layer, decreases monotonically with increasing density difference at the upper interface, and reaches its minimum in the limiting case of a vanishing density difference between the intermediate and bottom layers. However, as the wave amplitudes become larger than 50 m, no monotonic relation between density difference and wavelength is found (Figure 2).

4. Surface and Subsurface Jets Observed in the Strait of Messina

As in several other locations of the world's oceans [*Gargett,* 1976; *Farmer and Smith,* 1980; *Cummins and LeBlond,* 1984; *Farmer and Denton,* 1985; *Armi and Farmer,* 1988; *Wang et al.,* 1991], in the Strait of Messina, a narrow channel separating the Italian island of Sicily from the Italian peninsula (see Figure 3), internal waves are generated by the interaction of the semidiurnal tidal flow with the strait sill [*Alpers and Salusti,* 1983; *Griffa et al.,* 1986; *di Sarra et al.,* 1987; *Sapia and Salusti,* 1987; *Artale et al.,* 1990; *Nicolò and Salusti,* 1991; *Brandt et al.,* 1997, 1999]. During the Atlantic Ionian Stream '95 cruise (AIS95), aspects of the tidally induced internal dynamics were observed in high-resolution hydrographic and current data acquired north and south of the sill in the Strait of Messina [*Brandt et al.,* 1999]. The hydrographic data were obtained using a towed conductivity-temperature-depth (CTD) chain; the velocity data were obtained using a 75 kHz acoustic Doppler current profiler (ADCP) mounted on the vessel. The chain provided on-line data with a vertical and horizontal resolution of about 2.5 and 5 m, respectively, at a ship speed of 2.5 m s^{-1}. The temperature was measured with an accuracy of 0.01 K, and the salinity was measured with an accuracy of 0.02. The current data were recorded in vertical bins of 8 m with a horizontal resolution of about 150 m at a ship speed of

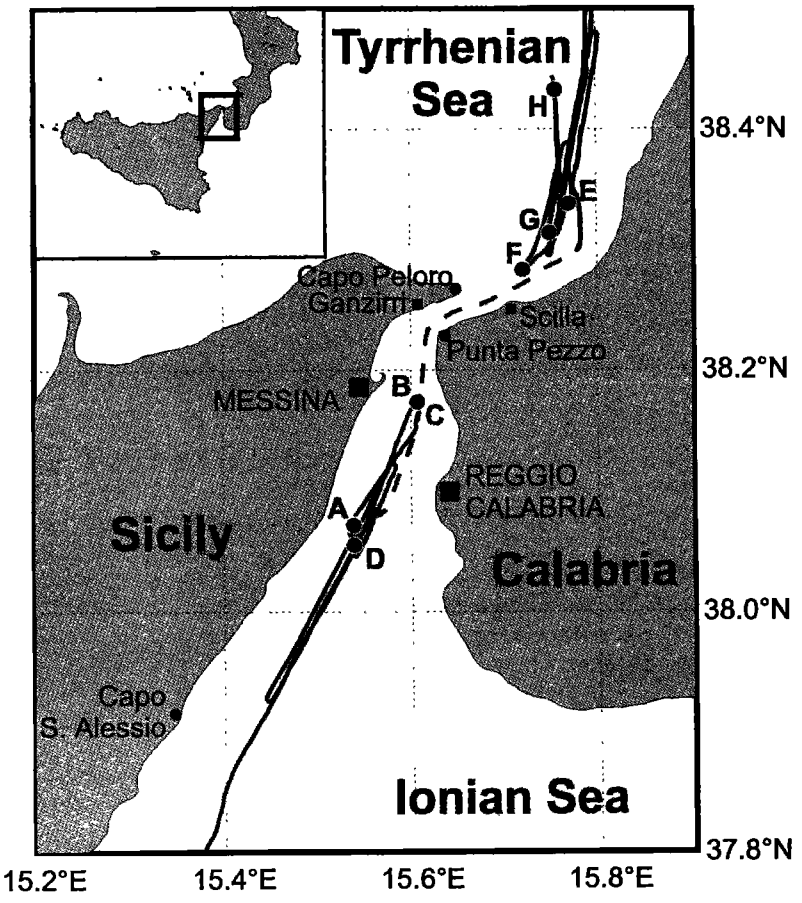

Figure 3. Geographical map of the Strait of Messina in which the route followed by NRV *Alliance* during AIS95 (solid and dashed lines) is inserted. Solid lines mark the locations where measurements were carried out by using the CTD chain and the ADCP. The dashed line marks the locations where only ADCP measurements were carried out. Dots mark the starting points and the end points of the measurements shown in Plates 1-4. The sill of the Strait of Messina is located between Ganzirri and Punta Pezzo. The location of the Strait of Messina in the central Eurafrican Mediterranean basin is presented in the upper left corner.

2.5 m s^{-1}. The current speed was measured with an accuracy of 0.03 m s^{-1} for both horizontal and vertical components.

During the cruise, northward and southward directed water jets were observed that developed undulations evolving into large-amplitude internal solitary waves. The cause of these water jets is the predominantly semidiurnal tide, which is constricted in a narrow channel characterized by strong horizontal density gradients (note that this situation is similar to that occurring in the Laurentian Channel described by *Wang et al.* [1991]). During the period of investigation the surface water of the Tyrrhenian Sea north of the strait sill was heavier than the surface water of the Ionian Sea south of the strait sill. As a consequence, during northward tidal flow, surface water of the Ionian Sea spreads as a surface jet into the Tyrrhenian Sea, and during southward tidal flow, heavier surface water of the Tyrrhenian Sea spreads, after having sunk to a depth of about 100 m, as a subsurface jet into the Ionian Sea [*Brandt et al.*, 1999].

Plate 1 shows data acquired south of the strait sill, along the ship path from A to B marked in Figure 3. The measurements started at point A at 1925 UTC on October 24, 1995, i.e., 2 hours 14 min before the maximum southward tidal flow at Punta Pezzo occurred, and ended at point B at 2054 UTC. Plate 1 shows the density distribution measured by the CTD chain (Plate 1a), the distribution of the horizontal velocity field measured by the ADCP (Plate 1b), and the corresponding distribution of the Richardson number (Plate 1c) calculated from the observed density and velocity fields (note that for this purpose the velocity data were slightly smoothed along the vertical coordinate) according to

$$Ri = -\frac{g}{\rho_0}\frac{\partial \rho}{\partial z}\left[\left(\frac{\partial u}{\partial z}\right)^2 + \left(\frac{\partial v}{\partial z}\right)^2\right]^{-1}. \quad (7)$$

The density field (Plate 1a) shows the presence of a southward propagating internal bore. The pycnocline is depressed by about 40 m at its front, which is located ~8 km south of the strait sill. The distribution of the horizontal velocity field (Plate 1b) shows the presence of a subsurface jet with a maximum horizontal velocity of about 0.8 m s^{-1}. Its central depth is about 100 m, and its thickness is about 50 m. Vertical mixing estimated from the distribution of the Richardson number (Plate 1c) is, in general, large throughout the region. This is not surprising as the data refer to a very energetic oceanic area characterized by the presence of

vigorous horizontal and vertical currents [*Vercelli,* 1925; *Defant,* 1940, 1961]. In particular, we note that Richardson numbers lower than 0.25 are found especially in the near-surface layer, where a very weak stratification is present, and before the internal bore front, where a strong vertical shear velocity can be observed. The strong vertical shear induced by the bore does not seem, instead, to give rise to large vertical mixing as it is associated with a large vertical density gradient. Thus the data shown in Plate 1 provide the picture of an early stage of the structure of a strong intermediate water jet associated with a step-like depression of the pycnocline in an environment characterized by strong turbulent mixing.

The further evolution of this oceanic feature is illustrated in Plate 2, which shows data acquired <1 hour later south of the strait sill, along the ship path from C to D marked in Figure 3. The measurements started at point C at 2101 UTC on October 24, 1995, i.e., 38 min before the maximum southward tidal flow at Punta Pezzo occurred, and ended at point D at 2232 UTC. The step-like disturbance developed into an undular bore characterized by a leading wave of more than 50 m amplitude (Plate 2a). Characteristics of the bore undulations are also evident in the structure of the velocity field (Plate 2b). As in the previous case, small values of the Richardson number are found throughout the region (Plate 2c). Note, however, that while at the rear of the water jet (in correspondence to an area of very small-scale density fluctuations (see Plate 2a)) an extended patch of low Richardson numbers is evident, the larger-scale undulations at the head of the jet are connected to patches of larger Richardson numbers, indicating smaller turbulent mixing.

Plate 3 presents data acquired north of the strait sill, along the ship path from E to F marked in Figure 3. The measurements started at point E at 1527 UTC on October 25, 1995, i.e., 35 min before the maximum northward tidal flow at Punta Pezzo occurred, and ended at point F at 1614 UTC. The density field (Plate 3a) shows the presence of a northward propagating internal undular bore. Three well-developed, rank-ordered, large-amplitude internal solitary waves are visible, which are connected to a vigorous surface water jet (Plate 3b). Similar to the previous case, the waves propagate in a region characterized by low Richardson numbers (Plate 3c), but they are associated with patches of larger Richardson numbers, indicating smaller turbulent mixing. We note that in this case a large patch of low Richardson numbers can be observed within the jet. The further evolution of the undular bore is illustrated in Plate 4, which shows data acquired north of the strait sill, along the ship path from G to H marked in Figure 3. The measurements started at point G at 1830 UTC on October 25, 1995, and ended at point H at 1954 UTC. The three leading disturbances (Plate 4a) are no longer connected to the parent water jet (Plate 4b) and travel northward as independent internal solitary waves. These waves are now located in the Tyrrhenian Sea, outside the sill area. Accordingly, the wave propagation area is characterized by lower turbulent mixing. The patch of low Richardson numbers within the leading internal solitary wave (Plate 4c) may be a consequence of the fact that its upper part is composed of almost homogeneous water.

The dynamic picture of the tidally induced circulation in the Strait of Messina that emerges from the analysis of our data corresponds to the picture presented by *Defant* [1940, 1961]: Strong surface and subsurface water jets are generated periodically, which transport Ionian water into the Tyrrhenian Sea and Tyrrhenian water into the Ionian Sea. These jets can be interpreted as manifestations of the internal tide in the Strait of Messina but also as intrusions of a water mass at the top of another water mass (this case corresponds to our observations north of the Strait of Messina) or between two different water masses (this case corresponds to our observations south of the Strait of Messina). As these jets are caused by the tide constricted in a narrow channel characterized by strong horizontal density gradients, their density and velocity structures must be highly variable in space and time. In any case, because of the joint effect of amplitude and phase dispersion, undulations are generated, which eventually leave the parent jets and propagate for long distances as trains of internal solitary waves [*Brandt et al.,* 1997].

5. Numerical Simulations of Surface and Subsurface Water Jets

In the following we will investigate aspects of the dynamics of bore-like water jets, especially their disintegration into trains of internal solitary waves. Our study will focus on the description of subsurface jets in a three-layer ocean. However, at the end of this section we will also present results referring to surface jets in a two-layer ocean. In a control run, inspired by the analysis of the data collected south of the Strait of Messina presented in section 4, we will try to reproduce aspects of the observed dynamics. We will then explore the behavior of nonlinear, weakly nonhydrostatic subsurface jets by varying different parameters that characterize these oceanic features. The simulation carried out using a two-layer system will refer to the situation observed north of the Strait of Messina.

5.1. Simulation of a Subsurface Jet Inspired by the Analysis of the Data Collected South of the Strait of Messina

In the control run we approximate the stratification observed south of the strait sill by a three-layer system as depicted in the uppermost panel of Figure 4. On the left part of the domain the surface and the intermediate layer have a thickness of 80 and 50 m, respectively, while on the right part of the domain they have a thickness of 55 and 30 m, respectively. The interfaces describing the transition between the two different regions were assumed to have the form of a hyperbolic tangent. In the simulations presented in this section the total water depth was set to 800 m (note that only the upper 200 m are shown in Figure 4). The relative density difference across both interfaces was assumed to be 1.2×10^{-3}. In accordance with the measurements carried out south of the Strait of Messina, on the right part of the surface layer an initial current $U_1 = -0.3$ m s^{-1} flowing from right to left was assumed, while in the left part of the intermediate layer an initial current $U_2 = 0.8$ m s^{-1} flowing from left to right was assumed. Additional currents were assumed in the intermediate and in the bottom layers in order to ensure mass conservation as well as zero barotropic flow throughout the integration domain. The conditions used to initialize our model are thus

$$h_1 = H_{II} + (H_{I,} - H_{II})\frac{\tanh(x/L)+1}{2}, \qquad (8)$$

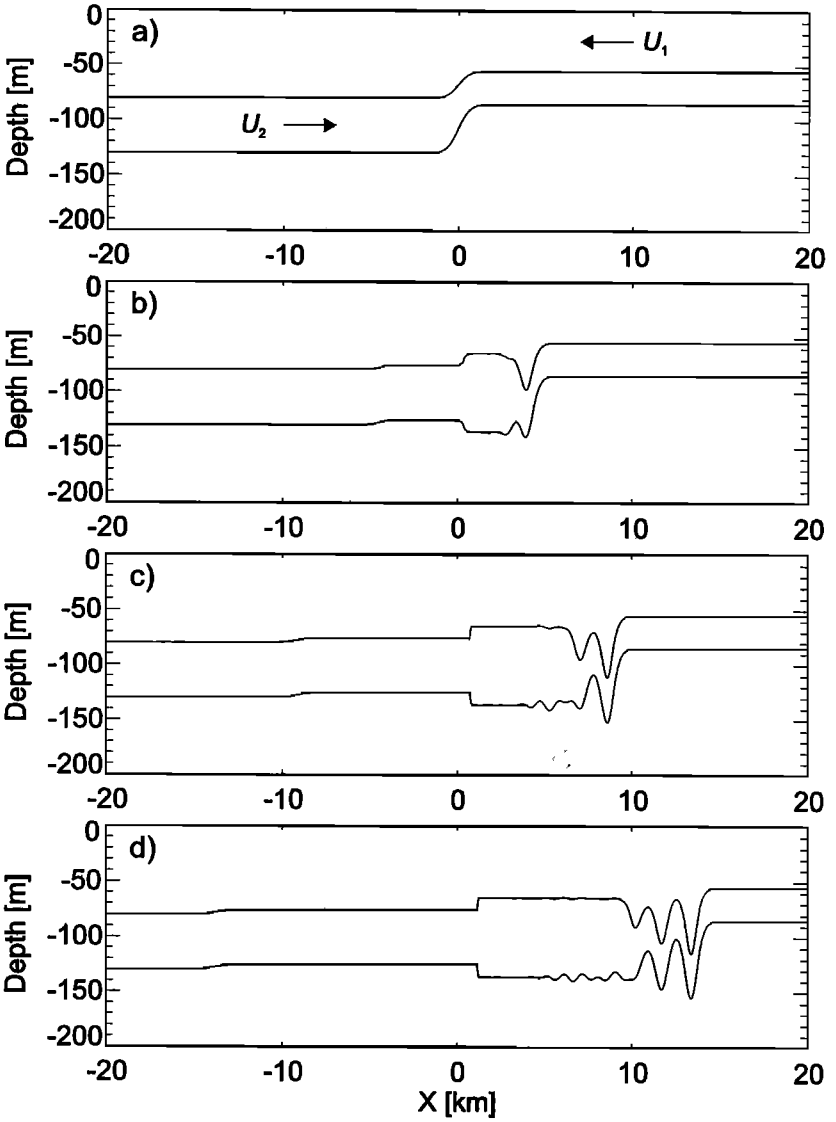

Figure 4. Form of the two interfaces in a three-layer system schematizing the stratification observed south of the Strait of Messina for (a) $t = 0$, (b) $t = 1$ hour, (c) $t = 2$ hours, and (d) $t = 3$ hours. This simulation was carried out using the following values of the parameters defining the model initial conditions in accordance with (8)-(12): $U_1 = -0.3$ m s^{-1}, $U_2 = 0.8$ m s^{-1}, $H_{1l} = 80$ m, $H_{2l} = 50$ m, $H_{1r} = 55$ m, $H_{2r} = 30$ m, and $L = 667$ m.

$$h_2 = H_{2l} + (H_{2r} - H_{2l})\frac{\tanh(x/L)+1}{2}, \tag{9}$$

$$\bar{u}_1 = U_1\frac{H_{1l} - h_1}{H_{1l} - H_{1r}}, \tag{10}$$

$$\bar{u}_2 = U_2\frac{h_3 - H_{3r}}{H_{3l} - H_{3r}} - \bar{u}_1\frac{h_1}{h_2 + h_3}, \tag{11}$$

$$\bar{u}_3 = -U_2\frac{h_3 - H_{3r}}{H_{3l} - H_{3r}}\frac{h_2}{h_3} - \bar{u}_1\frac{h_1}{h_2 + h_3}, \tag{12}$$

where H_{ir} and H_{il} $(i = 1,2,3)$ denote the initial layer thicknesses at the right and left model boundaries, respectively, and L represents the frontal width. The control run was carried out assuming $L = 667$ m. The coefficient of the horizontal momentum diffusion was set to 5 m^2 s^{-1}.

Figure 4 shows the temporal and spatial evolution of the two interfaces as simulated by our numerical model under the initial conditions mentioned above. The initial intermediate water jet develops into an undular bore composed of rank-ordered undulations followed by small-amplitude internal waves. After 1 hour of simulation (Figure 4b) the bore appears similar to that observed south of the strait sill (Figure 3). One hour later (Figure 4c), it has developed two well-distinguished undulations followed by smaller waves, and, again, it resembles remarkably the observed bore (Plate 1). Note that while the number of the observed and simulated internal waves agree quite well, our numerical model tends to overestimate the wave amplitudes. This results mainly from the fact that in our numerical model, interface and bottom friction are neglected. Moreover, as our numerical model does not include the effect of a varying channel width,

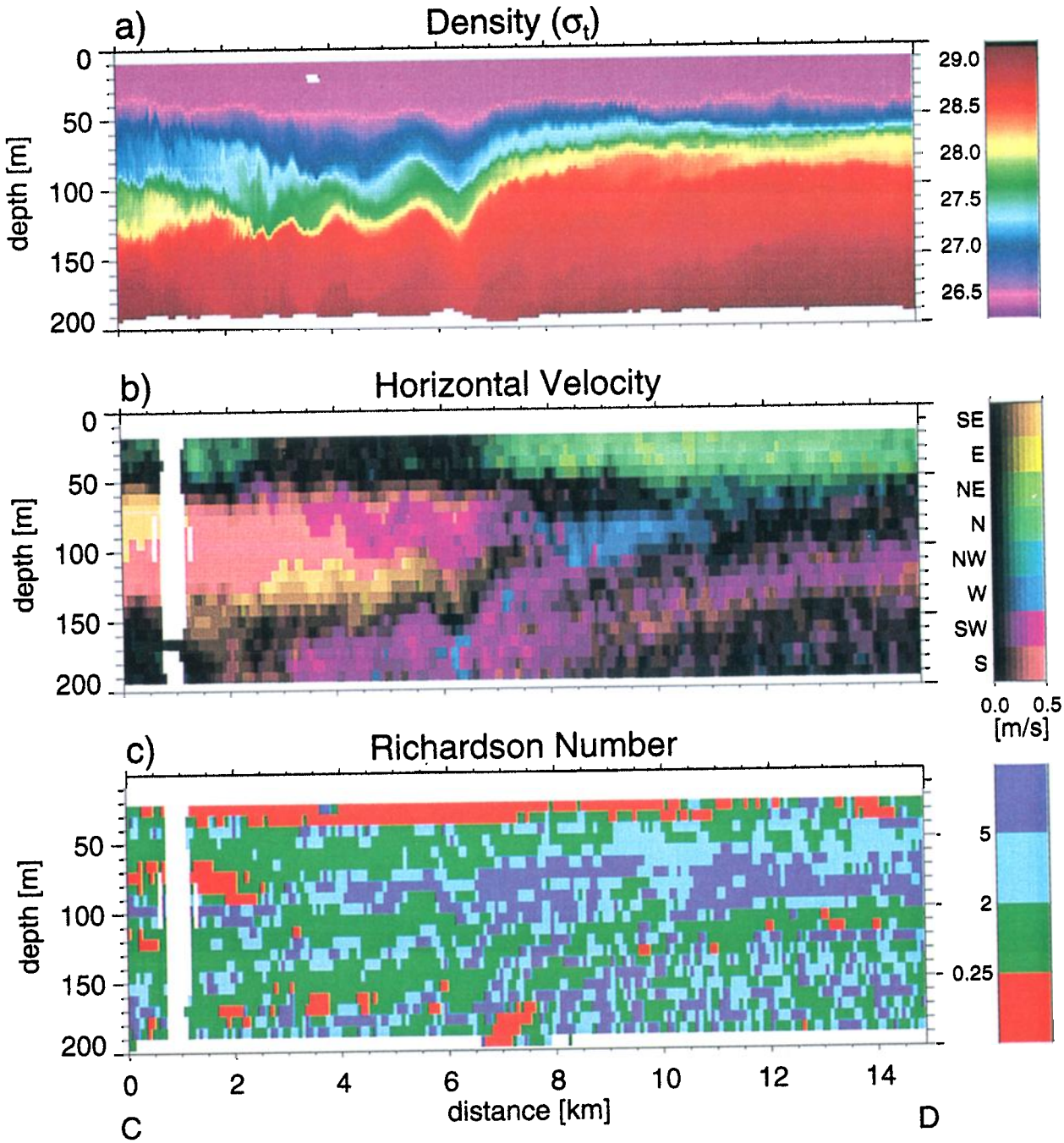

Plate 2. (a) Density distribution measured by the CTD chain, (b) distribution of the horizontal velocity field measured by the ADCP, and (c) distribution of the Richardson number between the positions C and D marked in Figure 3. In Plate 2b the colors represent the different directions of the horizontal velocity, while their brightness represents the velocity strength.

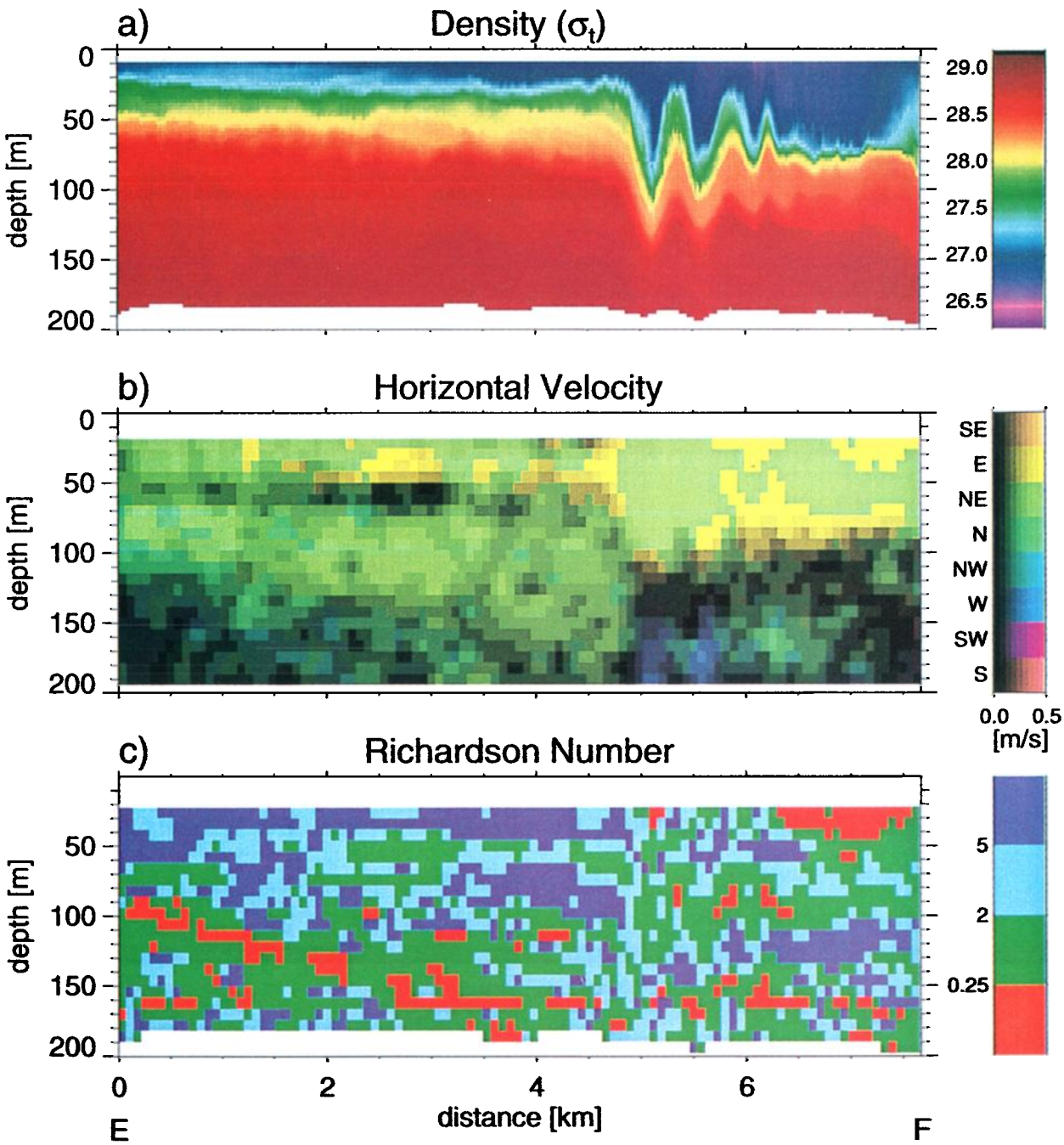

Plate 3. (a) Density distribution measured by the CTD chain, (b) distribution of the horizontal velocity field measured by the ADCP, and (c) distribution of the Richardson number between the positions E and F marked in Figure 3. In Plate 3b the colors represent the different directions of the horizontal velocity, while their brightness represents the velocity strength.

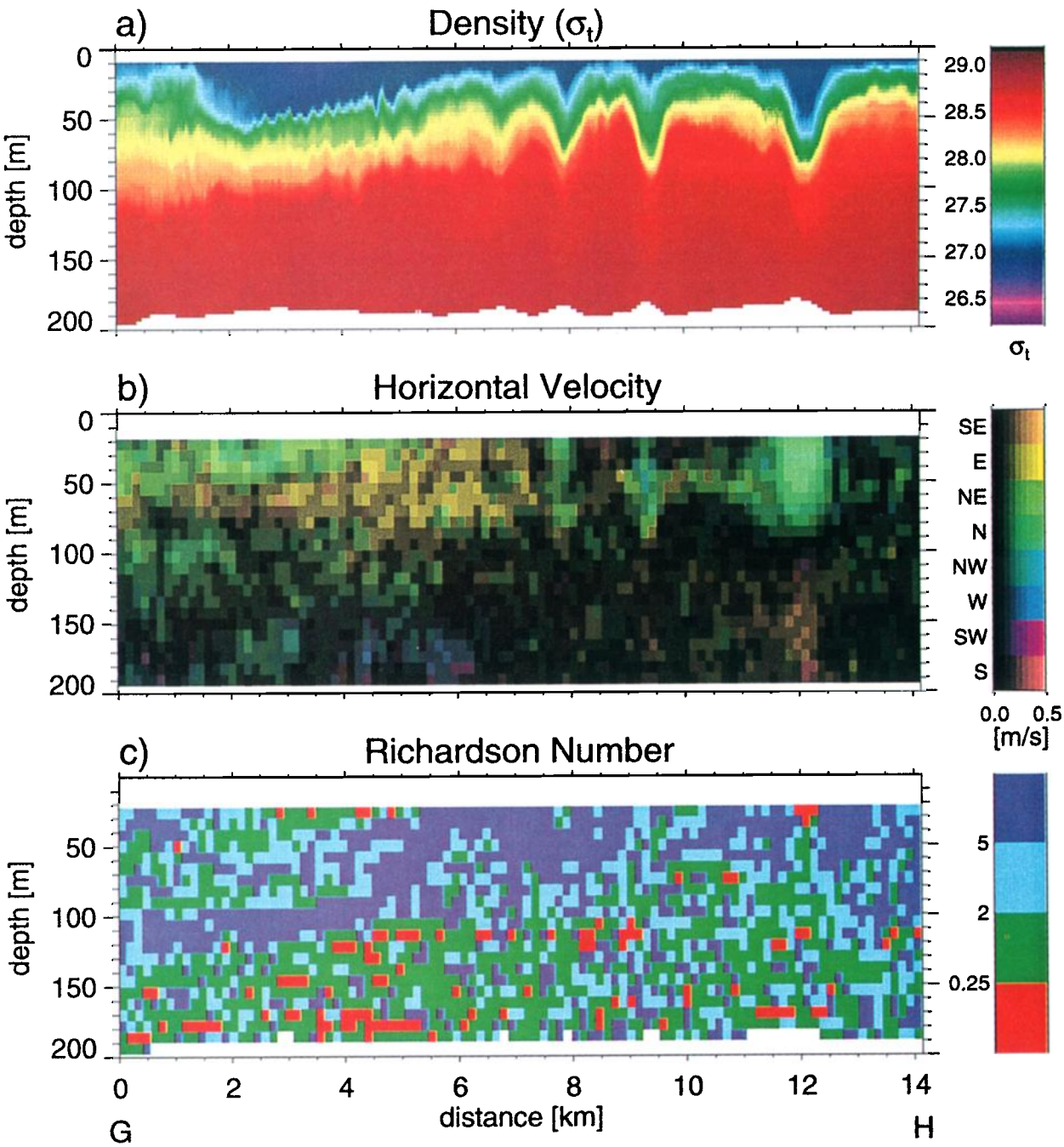

Plate 4. (a) Density distribution measured by the CTD chain, (b) distribution of the horizontal velocity field measured by the ADCP, and (c) distribution of the Richardson number between the positions G and H marked in Figure 3. In Plate 4b the colors represent the different directions of the horizontal velocity, while their brightness represents the velocity strength.

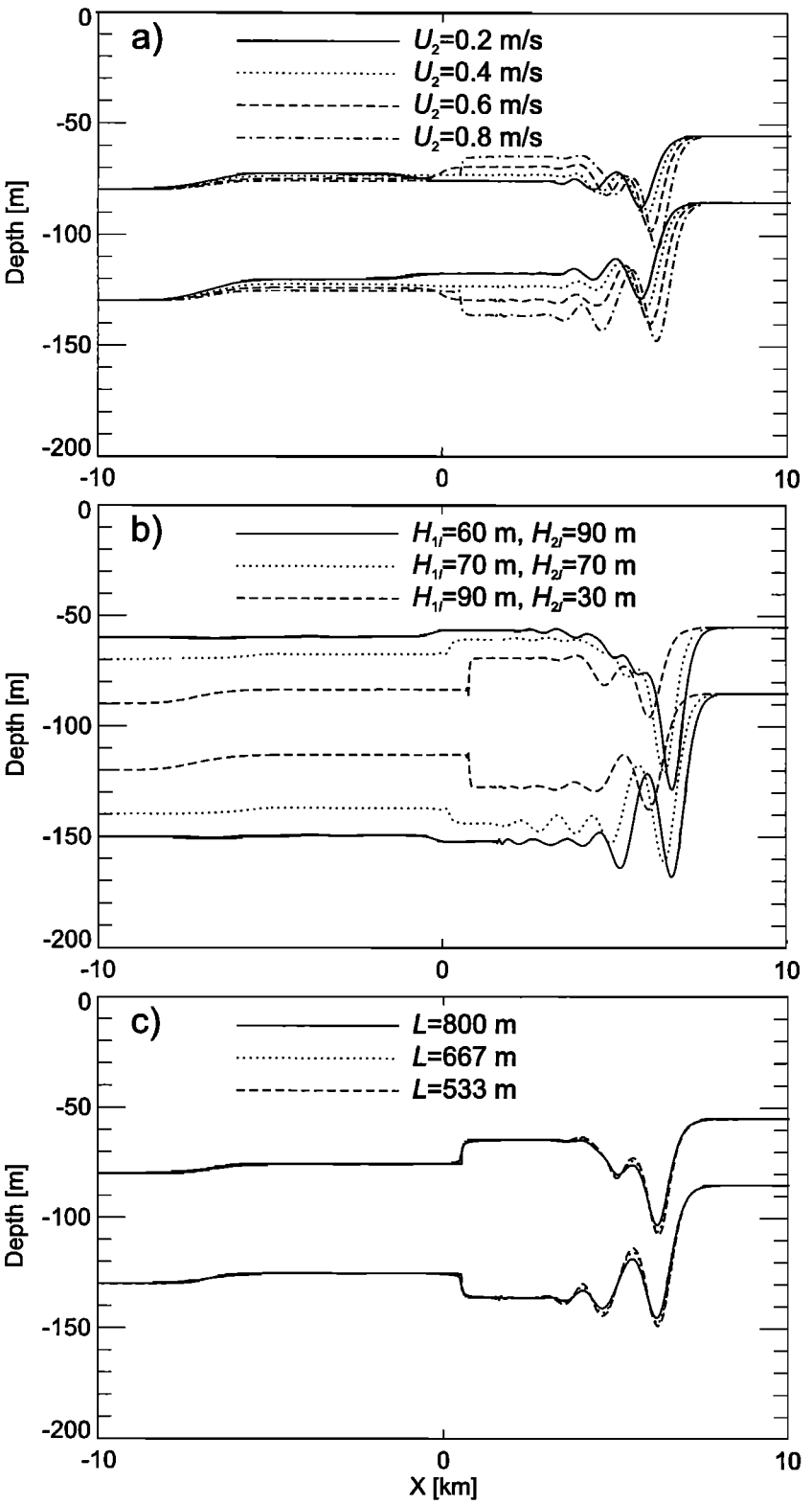

Figure 5. Dependence of the form of the two interfaces in a three-layer system (a) on U_2, (b) on H_{1l} and H_{2l}, and (c) on L after 1.5 hours of simulation. The remaining parameters are those characterizing the control run (see caption to Figure 4).

it cannot take into account the amplitude attenuation due to wave radial spreading, which, however, seems to be small in the southern part of the Strait of Messina as the radial spreading of internal waves is hindered there by the channel constriction. Note that a discrepancy between observed and simulated wave amplitudes can also result from the fact that our model considers only first-order phase dispersion [*Lamb and Yan*, 1996] and that Coriolis force is neglected in our

model. Our numerical model predicts also a broadening of the intermediate layer behind the wave train.

5.2. Sensitivity Studies

In this section we investigate the dependence of several characteristics of simulated nonlinear, weakly nonhydrostatic subsurface jets on initial surface and intermediate layer velocities, on intermediate layer thickness, and on frontal width. Figure 5 shows the dependence of the form of the two interfaces (a) on U_2, (b) on H_{1I} and H_{2I}, and (c) on L after 1.5 hours of simulation. The remaining parameters are those characterizing the control run. Variations in the strength of the intermediate jet velocity (Figure 5a) yield mainly variations in the amplitude of the resulting undulations as well as variations in the intermediate layer thickness and in the mean intermediate layer depth behind the jet front. The last two effects can be considered as the expression of second-mode and first-mode internal waves propagating against the water jet. Note that for large jet velocities (e.g., $U_2 = 0.8$ m s^{-1}) these second-mode waves (the expression for their linear phase speed is given in Appendix A) move to the right as the jet advection prevails against the wave propagation, while for small jet velocities (e.g., $U_2 = 0.2$ m s^{-1}) they move to the left. A variation in H_{1I} and H_{2I} (Figure 5b) results (together with a variation in the wave amplitudes, which, in this case, is mainly the consequence of the different positions of the two interfaces) in a remarkable variation in the broadening of the intermediate layer thickness behind the jet front. The small variations of the form of the simulated interfaces for different frontal widths (Figure 5c) indicate that this parameter (together with the corresponding initial velocity field across the wave front) contributes only marginally to the structure of the evolving jet. It mainly determines the time needed by the wave front to reach the equilibrium between nonlinear and dispersive effects. We carried out also sensitivity experiments aimed at investigating the dependence of the form of the two interfaces on different eddy viscosity coefficients: Our results indicate that in this case this dependence is negligible as its main effect consists only in a small decrease in the amplitudes of the simulated undulations.

In order to analyze further the influence of the strength of the currents in the upper and in the intermediate layers on the evolution of the simulated water jets we carried out three sets of numerical simulations considering three different values of U_1 (–0.1, –0.2, and –0.3 m s^{-1}). For each of these values, nine numerical simulations were carried out by increasing U_2 from 0.0 to 0.8 m s^{-1} in steps of 0.1 m s^{-1}. The dependence of the amplitude of the leading internal solitary wave of a wave train at the lower interface on the strength of the currents U_1 and U_2 is illustrated in Figure 6a, while the dependence of the distance separating the first two internal solitary waves of a wave train on the strength of the currents U_1 and U_2 is illustrated in Figure 6b. These internal wave parameters were

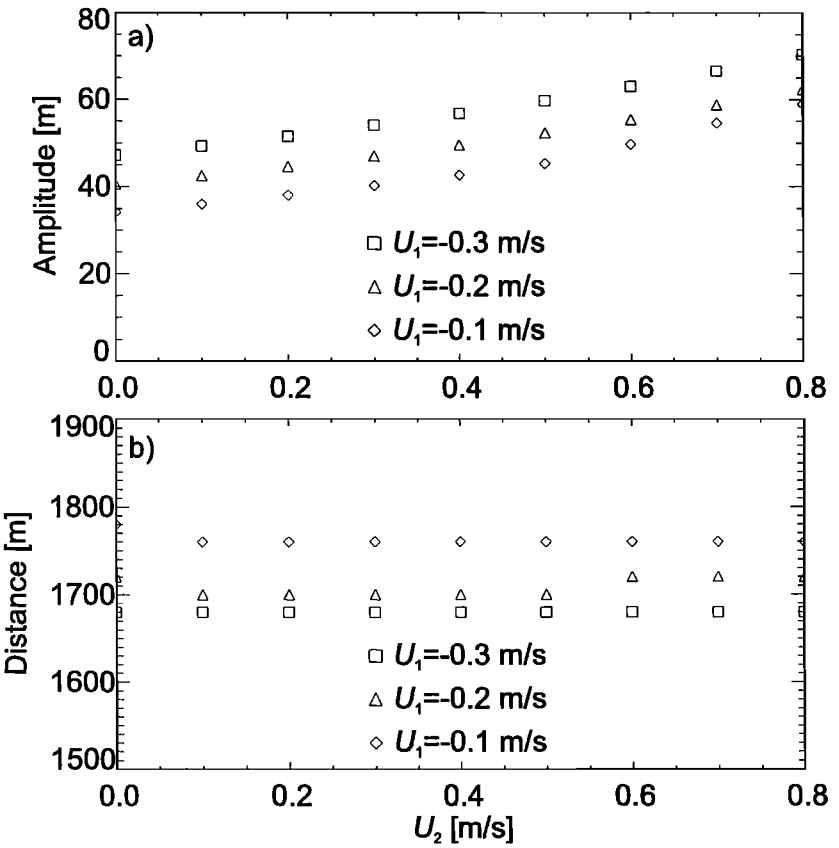

Figure 6. Dependence (a) of the amplitude of the leading internal solitary wave at the lower interface and (b) of the distance between the first two internal waves of a train of internal solitary waves in a three-layer system on the strength of the currents U_1 and U_2. Squares refer to $U_1 = -0.3$ m s^{-1}, triangles refer to $U_1 = -0.2$ m s^{-1}, and diamonds refer to $U_1 = -0.1$ m s^{-1}.

calculated from the simulated internal wave field after 3 hours of simulation. While increasing the values of U_1 and U_2 results in an increase of the wave amplitude, the distance between the first two internal solitary waves of a wave train is only very weakly dependent on the strength of the currents U_1 and U_2.

5.3. Simulation of a Subsurface Jet Inspired by the Analysis of the Data Collected North of the Strait of Messina

The initial form of the two-layer system referring to the northern stratification is depicted in Figure 7a. In the left part of the model domain the interface is located at 67 m depth, while in the right part of the model domain it is located at 7 m depth. As in the previous case, the transition between the interface depth of the two regions was assumed to have the form of a hyperbolic tangent, and the frontal width was assumed to be $L = 667$ m. The total water depth is 400 m, of which only the upper 200 m are shown in Figure 7. The relative density difference at the interface is 1.2×10^{-3}. In accordance with the measurements carried out north of the Strait of Messina, in the left part of the upper layer an initial current $U_1 = 0.8$ m s^{-1} flowing from left to right was assumed. The initial current in the bottom layer was then calculated from (5) using $h_3 \equiv 0$ and $\bar{u}_3 \equiv 0$ and imposing zero barotropic flow. The conditions used to initialize our model are

$$h_1 = H_{1l} + (H_{1r} - H_{1l})\frac{\tanh(x/L)+1}{2}, \tag{13}$$

$$\bar{u}_1 = U_1 \frac{h_1 - H_{1r}}{H_{1l} - H_{1r}}, \tag{14}$$

$$\bar{u}_2 = -\bar{u}_1 \frac{h_1}{h_2}. \tag{15}$$

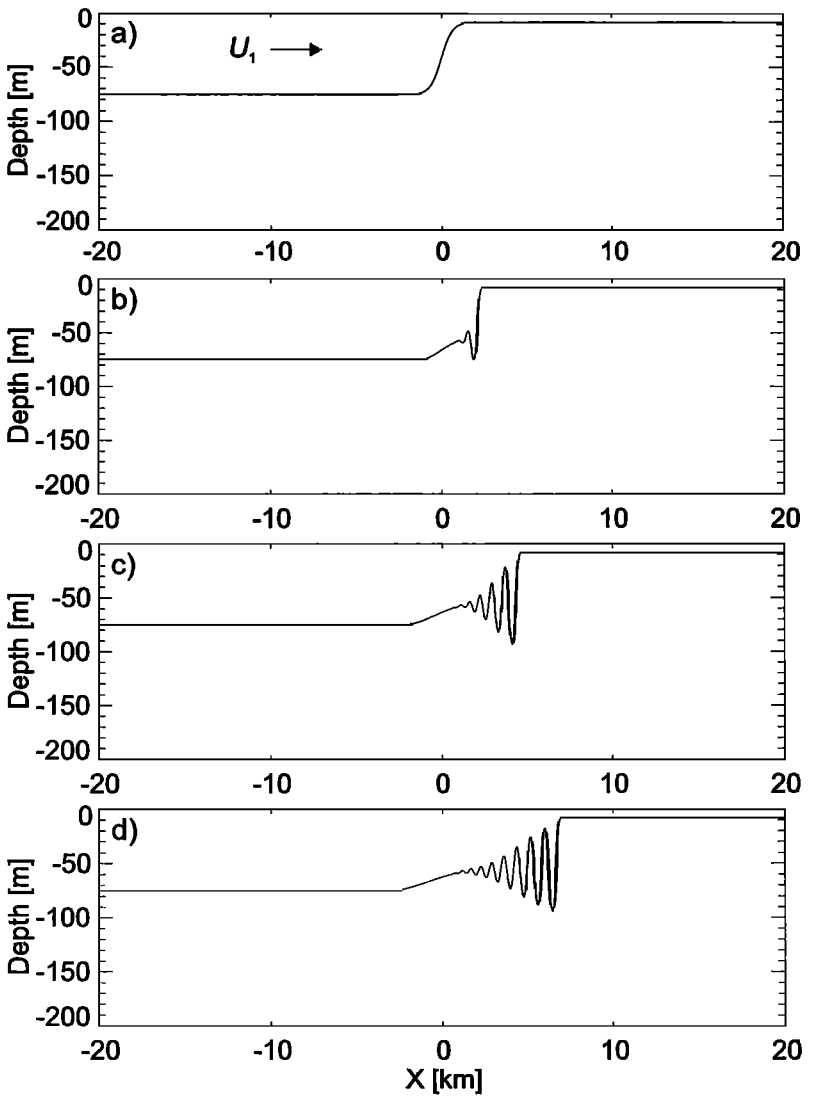

Figure 7. Form of the interface in a two-layer system schematizing the stratification observed north of the Strait of Messina for (a) $t = 0$, (b) $t = 0.5$ hours, (c) $t = 1$ hour, and (d) $t = 1.5$ hours. This simulation was carried out using the following values of the parameters defining the model initial conditions in accordance to (13)-(15): $U_1 = 0.8$ m s^{-1}, $H_{1l} = 77$ m, $H_{1r} = 7$ m, and $L = 667$ m.

The horizontal momentum diffusion was set to 5.0 $m^2 s^{-1}$. As shown in Figure 7, an almost immediate disintegration of the internal bore into a train of internal solitary waves occurs. In this case our numerical model clearly overestimates numbers and amplitudes of the internal waves (compare Figure 7c and Plate 3). This results mainly from the fact that while north of the strait sill the channel opens abruptly toward the Tyrrhenian Sea, thus leading to a strong wave attenuation due to radial spreading, our model is not able to describe channel width variations. Additional explanations are the neglect, in our model, of interface and bottom friction and Coriolis force. In order to analyze the influence of the strength of the current in the upper layer on the evolution of the internal waves, numerical simulations were carried out with U_1 increasing from 0.1 to 1.3 $m s^{-1}$ in steps of 0.1 $m s^{-1}$. The relation between the amplitude of the first internal solitary wave of the wave train and the strength of the current U_1 is depicted in Figure 8a; the relation between the distance separating the first two internal solitary waves of the wave train and the strength of the current U_1 is depicted in Figure 8b. These internal wave parameters were calculated from the simulated internal wave field after 1.5 hours of simulation. Both parameters show an almost linear dependence on the strength of the current U_1. Note that the variations imposed in the jet velocity result in large variations in the amplitude as well as in the distance between the first two waves of the simulated features.

6. Conclusions

In this study we investigated aspects of the dynamics of internal solitary waves using a new numerical three-layer model that solves the nonlinear, weakly nonhydrostatic Boussinesq equations and using high-resolution in situ data. Model applications were presented for two phenomena that cannot be described using a two-layer model. The first phenomenon concerns the propagation of internal solitary waves in an ocean where a shallow seasonal thermocline is superimposed on a two-layer permanent stratification. We found that for small to medium wave amplitudes a decrease in the strength of the upper pycnocline, which represents in our study a shallow seasonal thermocline superimposed on a two-layer permanent stratification, yields an increase in the simulated wavelengths, but for large wave amplitudes this dependence is no longer monotonic. The second phenomenon refers particularly to high-resolution observations made north and south of the Strait of Messina, where surface and subsurface jet-like water intrusions are generated by the complex interaction of the barotropic tide with the strait sill in a region characterized by a strong horizontal density gradient. Our observations indicate that from initial very energetic surface and subsurface jet-like intrusions subject to strong turbulent mixing, internal solitary waves emerge as robust, quasi-nondissipative oceanic features. To force our model, we imposed idealized flow conditions aimed at approximating

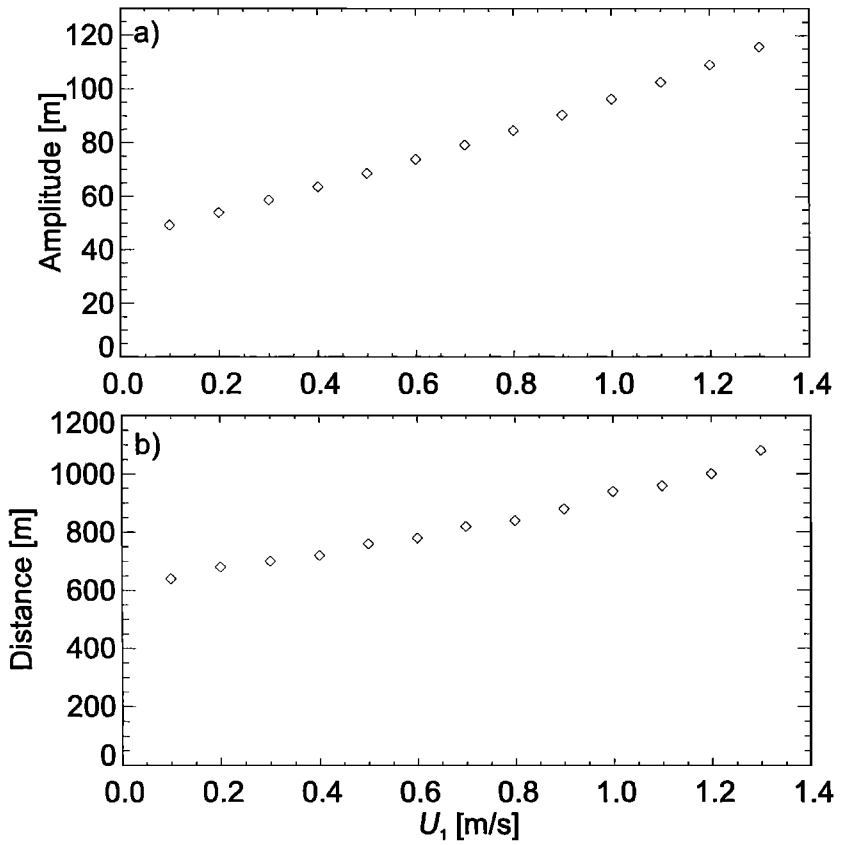

Figure 8. Dependence (a) of the amplitude of the leading internal solitary wave and (b) of the distance between the first two internal waves of a train of internal solitary waves in a two-layer system on the strength of the current U_1.

possible initial stages of the observed surface and subsurface water jets. The numerical model was able to capture different aspects of the observed wave fields. The velocity of a subsurface water jet, its layer thickness, and its frontal width were varied in order to elucidate the dependence of the form of the two interfaces of the three-layer model on these parameters. Variations in the strength of the intermediate jet velocity result in variations in the amplitude of the simulated undulations, in the intermediate layer thickness, and in the mean intermediate layer depth behind the jet front. A similar behavior is induced by variations in the intermediate layer thickness. This behavior accounts for the radiating nature of the simulated water jets: Given a certain interface and density configuration, it is conceivable that in analogy to a two-layer system an initial velocity field will exist for which no variations in the layer thicknesses behind the jet front will result. However, as our investigation was aimed at understanding aspects of the dynamics of surface and subsurface jets as they were observed in the approaches of the Strait of Messina, our main focus was the study of their highly variable behavior induced by perturbations of the flow and density field. In other words, the jets observed north and south of the Strait of Messina cannot be understood fully by describing them as mere long internal waves propagating away from the sill as the variability in their evolution induced by variable bottom topography, horizontal density variations, variable ambient currents, and differential mixing defines them as peculiar features of the complex ocean dynamics.

Appendix A

In order to develop expressions for first-mode and second-mode phase speeds of linear internal waves propagating in a three-layer system we consider the linear, hydrostatic, and inviscid form of the model equations (1)-(5):

$$\frac{\partial \bar{u}_2}{\partial t} - \frac{\partial \bar{u}_1}{\partial t} + g'_1 \frac{\partial \zeta_1}{\partial x} = 0, \tag{A1}$$

$$\frac{\partial \bar{u}_3}{\partial t} - \frac{\partial \bar{u}_2}{\partial t} + g'_2 \frac{\partial \zeta_2}{\partial x} = 0, \tag{A2}$$

$$\frac{\partial \zeta_1}{\partial t} - h_1 \frac{\partial}{\partial x} \bar{u}_1 = 0, \tag{A3}$$

$$\frac{\partial \zeta_2}{\partial t} + h_3 \frac{\partial}{\partial x} \bar{u}_3 = 0, \tag{A4}$$

$$h_1 \bar{u}_1 + h_2 \bar{u}_2 + h_3 \bar{u}_3 = 0. \tag{A5}$$

Note that in (A1)-(A5), h_i (i = (1,2,3)) denotes the undisturbed layer thickness of each layer. Moreover, the assumption of zero barotropic flow is introduced (compare (5) and (A5)). From (A1)-(A5) the following fourth-order differential equation can be obtained:

$$\frac{\partial^4 \bar{u}_1}{\partial t^4} - \frac{g'_1 h_1 (h_2 + h_3) + g'_2 h_3 (h_1 + h_2)}{h_1 + h_2 + h_3} \frac{\partial^4 \bar{u}_1}{\partial t^2 \partial x^2} + \frac{g'_1 g'_2 h_1 h_2 h_3}{h_1 + h_2 + h_3} \frac{\partial^4 \bar{u}_1}{\partial x^4} = 0. \tag{A6}$$

Equation (A6) can be expressed as follows:

$$\left(\frac{\partial^2}{\partial t^2} - c_1^2 \frac{\partial^2}{\partial x^2} \right) \left(\frac{\partial^2}{\partial t^2} - c_2^2 \frac{\partial^2}{\partial x^2} \right) \bar{u}_1 = 0, \tag{A7}$$

where c_1 and c_2 are the first-mode and second-mode phase speeds, respectively. Their values are

$$c_1 = \pm \left\{ \frac{1}{2} \frac{g'_1 h_1 (h_2 + h_3) + g'_2 h_3 (h_1 + h_2)}{h_1 + h_2 + h_3} + \left[\frac{1}{4} \left(\frac{g'_1 h_1 (h_2 + h_3) + g'_2 h_3 (h_1 + h_2)}{h_1 + h_2 + h_3} \right)^2 - \frac{g'_1 g'_2 h_1 h_2 h_3}{h_1 + h_2 + h_3} \right]^{1/2} \right\}^{1/2}, \tag{A8}$$

$$c_2 = \pm \left\{ \frac{1}{2} \frac{g'_1 h_1 (h_2 + h_3) + g'_2 h_3 (h_1 + h_2)}{h_1 + h_2 + h_3} - \left[\frac{1}{4} \left(\frac{g'_1 h_1 (h_2 + h_3) + g'_2 h_3 (h_1 + h_2)}{h_1 + h_2 + h_3} \right)^2 - \frac{g'_1 g'_2 h_1 h_2 h_3}{h_1 + h_2 + h_3} \right]^{1/2} \right\}^{1/2}. \tag{A9}$$

Acknowledgments. We would like to express our gratitude to Jürgen Sellschopp of the SACLANTCEN, La Spezia, Italy, to Heinz-Volker Fiekas of the Forschungsanstalt der Bundeswehr für Wasserschall- und Geophysik, Kiel, Germany, and to Detlef Quadfasel of the Niels Bohr Institute for Astronomy Physics and Geophysics, Copenhagen, Denmark. Their efforts made possible the realization of the in situ measurements. We thank Marcus Dengler for processing the ADCP data as well as the captain and crew of the NRV *Alliance* of the SACLANTCEN for their support during the experimental phase of this study. We would like to thank also the two anonymous reviewers of our manuscript for their helpful suggestions. This work was partly supported by the European Commission under contract MAS3-CT95-0027 and by the Deutsche Forschungsgemeinschaft in the frame of the Sonderforschungsbereich 512.

References

Alpers, W., Theory of radar imaging of internal waves, *Nature, 314*, 245-247, 1985.

Alpers, W., and E. Salusti, Scylla and Charybdis observed from space, *J. Geophys. Res., 88*, 1800-1808, 1983.

Apel, J.R., L.A. Ostrovsky, and Y.A. Stepanyants, Internal solitons in the ocean, *Tech. Rep. MERCJRA0695*, 70 pp., Milton S. Eisenhower Research Center, Applied Physics Laboratory, The John Hopkins University, John Hopkins Rd., Laurel, MD 20707, 1995.

Armi, L., and D.M. Farmer, The flow of Mediterranean water through the Strait of Gibraltar, *Prog. Oceanogr., 21*, 1-105, 1988.

Artale, V., D. Levi, S. Marullo, and R. Santolieri, Analysis of nonlinear internal waves observed by Landsat thematic mapper, *J. Geophys. Res., 95*, 16, 065-16, 073, 1990.

Brandt, P., W. Alpers, and J.O. Backhaus, Study of the generation and propagation of internal waves in the Strait of Gibraltar using a numerical model and synthetic aperture radar images of the European ERS 1 satellite, *J. Geophys. Res., 101*, 14,237-14,252, 1996.

Brandt, P., A. Rubino, W. Alpers, and J.O. Backhaus, Internal waves in the Strait of Messina studied by a numerical model and synthetic aperture radar images from the ERS 1/2 satellites, *J. Phys. Oceanogr., 27*, 648-663, 1997.

Brandt, P., A. Rubino, D. Quadfasel, W. Alpers, J. Sellschopp, and H.-V. Fiekas, Evidence for the influence of Atlantic-Ionian stream

fluctuations on the tidally induced internal dynamics in the Strait of Messina, *J. Phys. Oceanogr., 29*, 1071-1080, 1999.

Brown, D.J., and D.R. Christie, Fully nonlinear solitary waves in continuously stratified incompressible fluids, *Phys. Fluids, 10*, 2569-2586, 1998.

Cummins, P.F., and P.H. LeBlond, Analysis of internal solitary waves observed in Davis Straight, *Atmos. Ocean, 22*, 173-192, 1984.

Defant, A., Scylla und Charybdis und die Gezeitenströmungen in der Straße von Messina, *Ann. Hydrogr. u. Mar. Meteorol., 5*, 145-157, 1940.

Defant, A., *Physical Oceanography*, 2 vol., Pergamon, New York, 1961.

di Sarra, A., A. Pace, and E. Salusti, Long internal waves and columnar disturbances in the Strait of Messina, *J. Geophys. Res., 92*, 6495-6500, 1987.

Djordjevic, V D., and L.G. Redekopp, The fission and disintegration of internal solitary waves moving over two-dimensional topography, *J. Phys. Oceanogr., 8*, 1016-1024, 1978.

Farmer, D.M., and R.A. Denton, Hydraulic control of flow over the sill in Observatory Inlet, *J. Geophys. Res., 90*, 9051-9068, 1985.

Farmer, D.M., and J.D. Smith, Tidal interaction of stratified flow with a sill in Knight Inlet, *Deep Sea Res., Part A, 27*, 239-254, 1980.

Gargett, A.E., Generation of internal waves in the Strait of Georgia, British Columbia, *Deep Sea Res. Oceanogr. Abstr., 23*, 17-32, 1976.

Gerkema, T., A unified model for the generation and fission of internal tides in a rotating ocean, *J. Mar. Res., 54*, 421-450, 1996.

Griffa, A., S Marullo, R Santolieri, and A. Viola, Preliminary observations of large-amplitude tidal internal waves near the Strait of Messina, *Cont. Shelf Res., 6*, 677-687, 1986.

Grimshaw R., E. Pelinovsky, and T. Talipova, The modified Korteweg-de Vries equation in the theory of large-amplitude internal waves, *Nonlinear Proc. Geophys., 4*, 237-250, 1997.

Holloway, P., E. Pelinovsky, and T. Talipova, A generalized Korteweg-de Vries model of internal tide transformation in the coastal zone, *J. Geophys. Res., 104*, 18,333-18,350, 1999.

Koop, C.G., and G Butler, An investigation of internal solitary waves in a two-fluid system, *J Fluid Mech., 112*, 225-251, 1981.

Lamb, K.G., and L Yan, The evolution of internal wave undular bores: comparison of a fully nonlinear numerical model with weakly nonlinear theory, *J. Phys. Oceanogr., 26*, 2712-2734, 1996.

McCreary, J.P., S. Zhang, and S.R. Shetye, Coastal circulation driven by river outflow in a variable-density 1 ½-layer model, *J. Geophys. Res., 102*, 15,535-15,554, 1997.

Mei, C.C., *The Applied Dynamics of Ocean Surface Waves*, John Wiley, New York, 1983.

Miyata, M., Long internal waves of large amplitude, in *Nonlinear Water Waves*, edited by K. Horikawa and H. Maruo, pp. 399-406, Springer-Verlag, New York, 1988.

Nicolò, L., and E. Salusti, Field and satellite observations of large amplitude internal tidal wave trains south of the Strait of Messina, Mediterranean Sea, *Ann. Geophys., 9*, 534-539, 1991.

Ostrovsky, L.A., and Y.A. Stepanyants, Do internal solitons exist in the ocean?, *Rev. Geophys., 27*, 293-310, 1989.

Sapia, A., and E. Salusti, Observation of nonlinear internal solitary wave trains at the northern and southern mouths of the Strait of Messina, *Deep Sea Res., Part A, 34*, 1081-1092, 1987.

Terez, D.E., and O.M. Knio, Numerical simulations of large-amplitude internal solitary waves, *J. Fluid Mech., 362*, 53-82, 1998.

Vercelli, F., Il regime delle correnti e delle maree nello stretto di Messina. Commissione Internazionale del Mediterraneo, Campagne della R. Nave „Marsigli" negli anni 1922 e 1923, 209 pp., 1925.

Vlasenko, V., P. Brandt, and A. Rubino, The structure of large-amplitude internal solitary waves, *J. Phys. Oceanogr., 30*, 2172-2185, 2000.

Wang, J., R.G. Ingram, and L.A. Mysak, Variability of internal tides in the Laurentian Channel, *J. Geophys. Res., 96*, 16,859-16,875, 1991.

Whitham, G.B , *Linear and Nonlinear Waves*, 636 pp., John Wiley, New York, 1974.

A. Rubino, Institut für Meereskunde, Universität Hamburg, Troplowitzstr. 7, 22529 Hamburg, Germany. (rubino@ifm.uni-hamburg.de)

P. Brandt, Institut fur Meereskunde an der Universitat Kiel, Düsternbrooker Weg 20, 24105 Kiel, Germany (pbrandt@ifm.uni-kiel.de)

(Received May 8, 2001; revised May 22, 2001;
accepted May 22, 2001.)